Estimation of Curie-Point Depths and Heat Flow from Spectral Analysis of EMAG2 Magnetic Data in Cyprus Island

Eren Pamuk[*,1], İlkin Özsöz[2]

(1) Department of Geophysical Research, General Directorate of the Mineral Research & Exploration of Turkey, 06800, Ankara, Turkey

(2) Department of Marine Research, General Directorate of the Mineral Research & Exploration of Turkey, 06800, Ankara, Turkey

Abstract

This study aims to determine Curie point depth (CPD), Heat flow and the boundaries of geological structures of Cyprus Island using EMAG2 magnetic data. CPD values were calculated by applying spectral analysis technique to magnetic anomaly map divided into 60 blocks ($60{\times}60$ km^2). Then, different thermal conductivity values (K = 1, 1.5 and 2.5 Wm^{-1}K^{-1}) and heat flow values were calculated using CPD values. CPD values ranged from 12.4 km to 28.18 km, and heat flow values were calculated between 20 and 50 mW/m^2 for K = 1. Shallow CPD values (CPD < 15 km) were calculated in Polis, Morphou Bay, in the area between Larnaca and Famagusta and north of Kyrenia. Heat flow values are relatively high in these areas which can be researched in detail in terms of potential geothermal. In the final phase of the study, the boundaries of buried geological structures were determined by Analytic Signal (AS), Total Horizontal Derivative (THDR) and Tilt angle (TA) methods. Moho depth, Moho-Curie difference, 2D cross-correlation map of Moho and Curie depths and Earthquake distribution map are used for interpretation of the tectonic regime. Moho-Curie difference is roughly 0 and the 2D cross-correlation map produces higher (0.60-0.75) values in the southern part of the study area which might be evaluated as a passive crust. It is possible to say that few earthquakes are observed where the difference is around 0.

1. Introduction

Curie point is defined as the temperature at which the magnetization disappears. The Curie point depth (CPD) is known as the depth at which magnetic minerals in the crust move from a ferromagnetic state to a paramagnetic state under the influence of increasing temperature [Nagata, 1961; Mohammed et al., 2019]. CPD data is often used in determining the thermal structure of the crust and estimating potential geothermal areas. The method, developed by Okubo et al. [1985], was used for CPD prediction in this study.

There are many studies about CPD estimation. Njeudjang et al. [2020] estimated Curie point depth, heat flow and geothermal gradient parameters for the Adamawa volcanic region (northern Cameroon) using EMAG2 data. Kumar et al. [2020] used satellite-based remote sensing, gravity and magnetic data to determine potential Kimberlite regions in their study. Li et al. [2017] obtained the first global model of Curie-point depth (GCDM) from EMAG2 magnetic data. Arnaiz-Rodríguez and Orihuela [2013] conducted CPD calculations for Venezuela and the Eastern Caribbean using the Enhanced Magnetic Model (EMM2010). For Eastern and South-eastern Asia Li and Wang [2016] investigated magnetic, heat flow and gravity data and their implications on deep crustal and uppermost mantle structures. Xu et al. [2017] determined CPD values from the magnetic anomaly data of EMAG2 in North China. Pamuk [2019] calculated CPD and heat flow values for the northern part of Eastern Anatolia, Turkey using EMAG2 magnetic data in his study. Özsöz [2021] estimated depth to the Curie isotherm in the Eastern Mediterranean Region with 39 sub-blocks using the World Digital Magnetic Anomaly Map (WDMAM) to reveal differences in thermal characteristics of the northern and southern part of the study area. Özer et al. [2022] investigated tectonic properties of Erzurum (Eastern Turkey) using CPD, heat flow and seismological data.
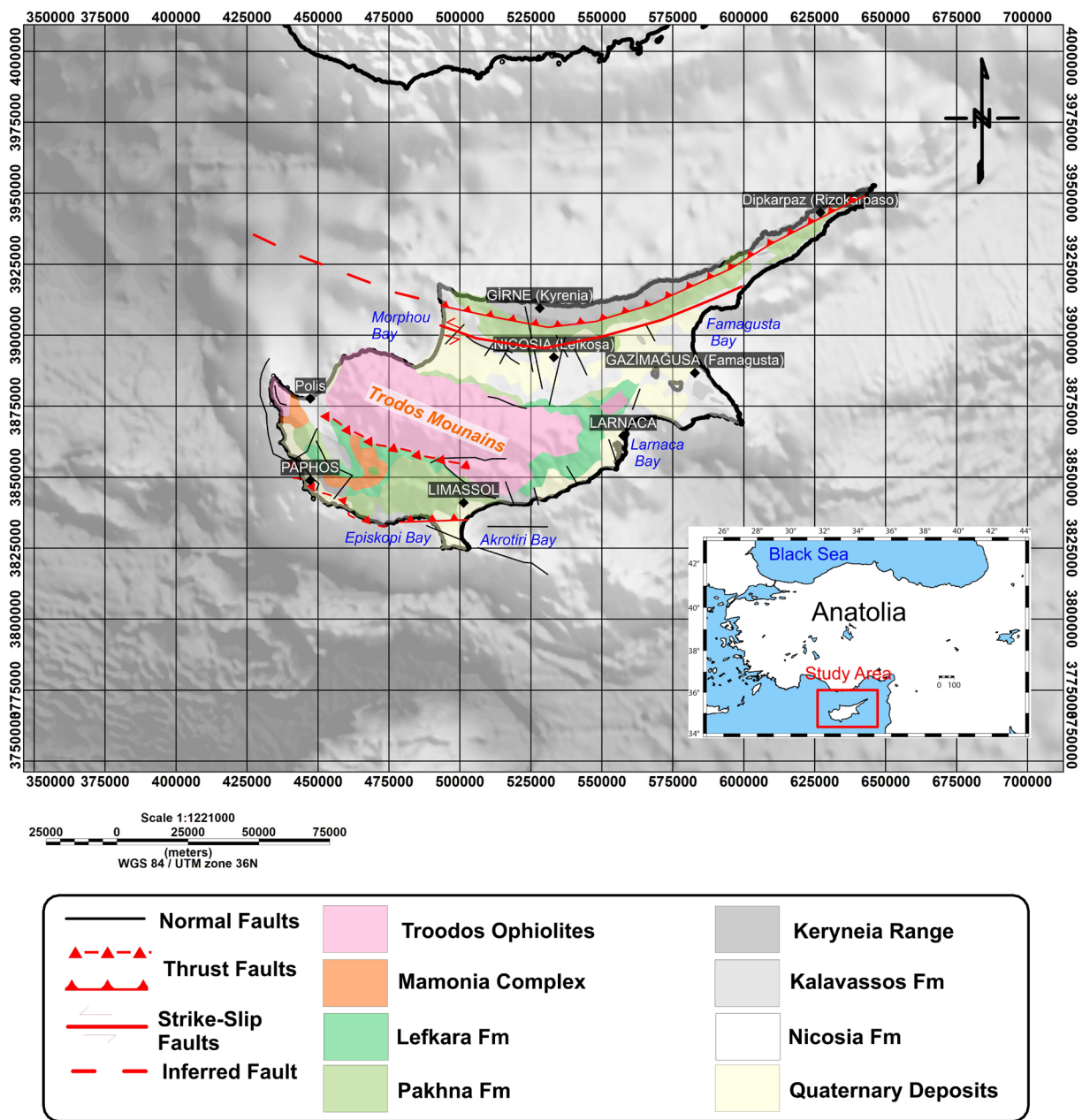

Figure 1. Simplified tectonic and geological map of Cyprus Island [modified from Symeou, 2018; the faults obtained from Symeou, 2018; Cagnan and Tanircan, 2010].

As it can be seen from previous studies, global magnetic maps such as the EMAG2 are quite advantageous in CPD value estimation due to the wide coverage. The EMAG2 stands for Earth Magnetic Anomaly Grid and it comprises ship, airborne and satellite magnetic measurements. In this study, the EMAG2 has been used to estimate depth to the Curie isotherm in and around Cyprus Island.

Numerous studies were carried out in Cyprus in terms of earth sciences. We can list some of them as follows. Cagnan and Tanircan [2010] conducted probabilistic seismic hazard analysis for Cyprus in their study. Asim et al. [2020] conducted a seismicity analysis for Cyprus. Ulutas [2020] analyzed the spread, altitude and arrival times of a possible tsunami for Cyprus in his study. Zissimos et al. [2019] investigated the spatial distribution of soil inorganic carbon (SIC) and soil organic carbon (SOC) across Cyprus. McPhee and Hinsbergen [2019] examined the structural and tectonic history of Cyprus. Elmas [2018] determined the structural discontinuities of Cyprus Island by applying total horizontal derivative and tilt angle techniques to satellite gravity and vertical first derivative data.

Cyprus Island can be considered a natural laboratory in terms of its geological importance. The convergent plate margin in the study area provides essential information about young mountain belts which can be related to the oceanic crust. Cyprus Island is located at the intersection of the platform of the African and Eurasian plates approaching each other. The margin between African and Anatolian plates can be defined by the Cyprus Arc where complex bathymetric structural trends are observed [Ergün et al., 2003]. Makris et al., [1983] and Robertson [1998] showed that the northern edge of the plate margin has fairly complex characteristics. The western part of the margin, Herodotus abyssal plain, is characterised by deep water which indicates stable crust whereas the eastern part of the boundary has a more variable crust. The subduction regime in the Cyprus Arc is in the transition phase to collision regime due to the thicker and less dense crust, in the northern boundary of the African plate [Kempler and Ben-Avraham, 1987; Robertson, 1998].

Destructive earthquakes were observed in Cyprus Island, which can be characterised as active and complex neotectonic history [Harrison et al., 2004]. The Troodos Massif in Cyprus Island is one of the largest ophiolite complexes in the region. There are numerous studies on the Troodos Massif [Harrison et al., 2004]. The formation and development of Troodos Ophiolite covers the Cenomanian-Turonian (92-90My) time interval [Mukasa and Ludden, 1987; Staudigel et al., 1986; Blome and Irwin, 1985; Hakyemez, 2014]. This ophiolite consists of serpentinite, harzburgite, dunite, gabbro, diabase and basalts [Kinnaird 2008, Symeou 2018]. Mamonia Complex, located in the southernmost part of Cyprus Island, consists of deformed sedimentary and volcanic rocks. The ages of these units vary from Triassic to Lower Cretaceous [Swarbrick and Robertson 1980; McPhee et. al. 2019]. The Kyrenia range, consisting of massif limestone bands, recrystallized limestones, dolomites and flysch, is between the Permian and Lower Cretaceous ages [Montadert et al., 2014; Symeou, 2018]. The Kalavasos Formation is the upper Miocene-aged sediments and has been characterised with gypsum deposits alternating with chalky marls and marly chalks [Symeou, 2018] (Figure 1).

In this paper, it is attempted to focus on estimating Curie Point Depth (CPD) and heat flow values for Cyprus Island via spectral analysis of the EMAG2 data set. Furthermore, boundaries of the subsurface geological structures and tectonic activity are interpreted by TA (tilt angle), AS (analytic signal), THDR (total horizontal derivative) and Moho-Curie comparison and the spatial distribution of earthquakes (M > 2.5).

2. Data and Methods

2.1 EMAG2 Magnetic Data

In this study, the magnetic data used in CPD, heat flow and boundary analysis is EMAG2 (global earth magnetic anomaly grid (2-arc-minute)) data, which is a compilation of measurements collected from satellite, sea and air [Maus et al., 2009]. The approximate resolution of EMAG2 data is 2 arc minutes. The magnetic anomaly grid is given for an altitude of about 4 km above sea level [Maus et al., 2009]. The processing sequence of the EMAG2 includes 5 steps: (1) grid merging, (2) airborne and ship magnetic data processing, (3) line levelling, (4) using an anisotropic correlation model over the oceans and (5) replacing the longest wavelength data (≥ 330 km) with MF 6 model [Maus et al., 2008]. EMAG2 provides wide opportunities such as testing tectonic hypotheses, investigating tectonic-structural relationships, generating plate reconstruction models and estimating CPD.

The EMAG2 magnetic anomaly map obtained for the study area is given in Figure 2a. Reduced to the north magnetic pole (RTP) was applied to the total magnetic anomaly values to eliminate bipolarity, and the obtained magnetic anomaly map is shown in Figure 2b.
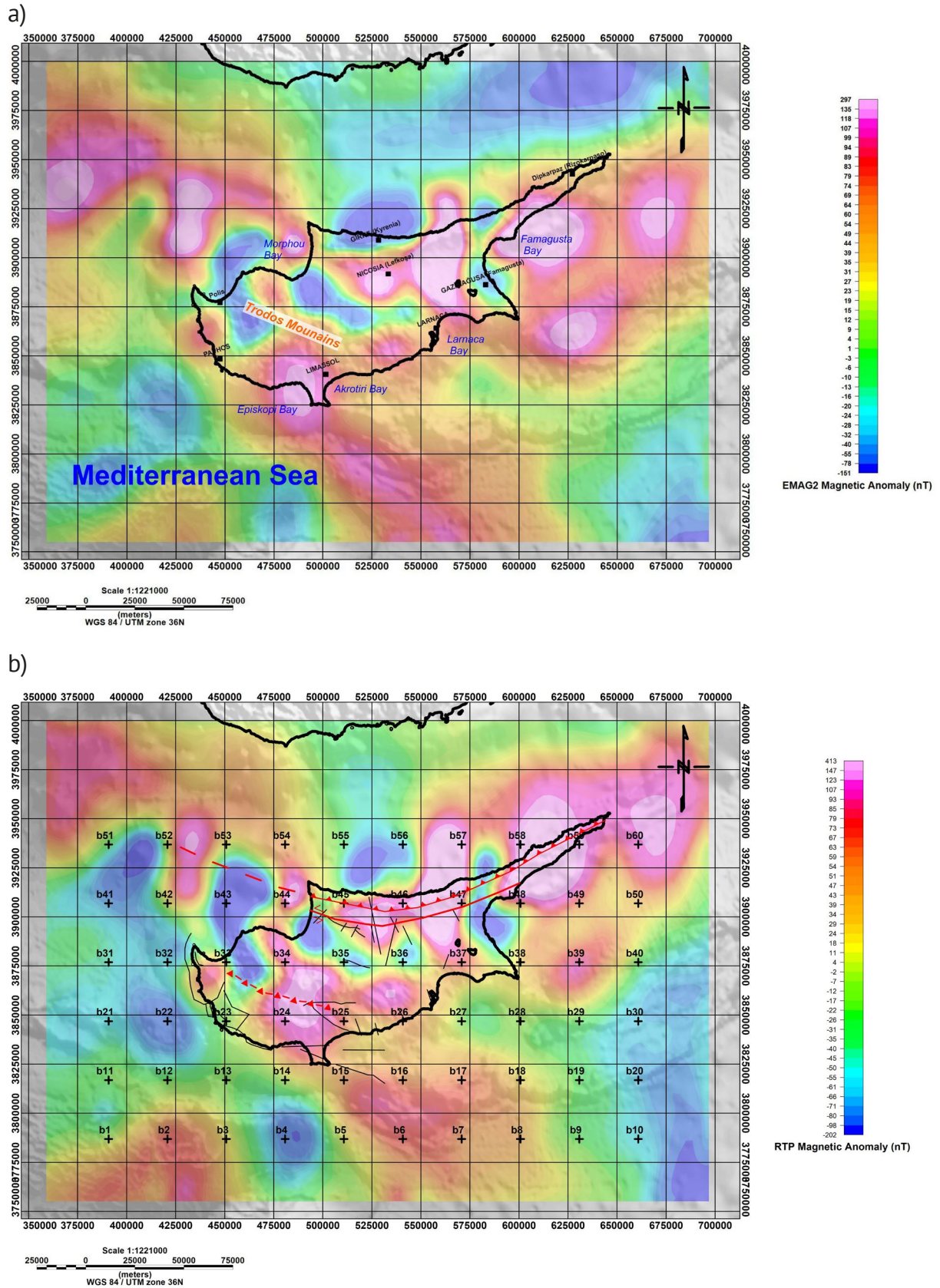
a)

b)

Figure 2. a) EMAG2 total field magnetic anomaly map [compiled from Maus et al., 2009], b) RTP total magnetic anomaly map with major tectonic structures in the study area (the black plus show the block centers used in the CPD calculation).

2.2 Earthquake Data

Spatial distribution of earthquakes in the study area is obtained from USGS Earthquake Catalogue [USGS, 2021]. During the earthquake selection, the study area is slightly expanded to evaluate the region on large scale. Additionally, all earthquakes between 1900 and 2020 whose magnitudes are higher than 2.5 are plotted. Focal depths of the earthquake events are not constrained.

2.3 Calculation of Curie Point Depth and Heat Flow

The radially averaged power spectrum procedure which provides depth to the top of the magnetic layer was introduced by Spector and Grant [1970]. Additionally, this method was improved by Treitel et al. [1971], Bhattacharyya and Leu [1975], Connard et al. [1983], Okubo et al. [1985], Blakely [1995], Tanaka et al. [1999], Ravat [2004] and Ross et al. [2006]. These methods allow the thermal structure of a region to be obtained by using magnetic anomaly values. A simplified definition of the radially averaged spectrum can be given as:

$$P(|k|) = Ae^{-2|k|z_t}\left(1 - e^{-|k|(z_b-z_t)}\right)^2 \tag{1}$$

where A is constant, k is wavenumber and z_b and z_t are depth to the top and the bottom of the magnetic source. Applying the natural logarithm to both sides of equation 1 leads to:

$$\ln[P(|k|)] = \ln[A] - 2z_t(k) + 2\ln\left[1 - e^{-|k|(z_b-z_t)}\right] \tag{2}$$

For high and medium values of wavenumber components, the exponential part in equation 2 can be ignored. Consequently, equation 2 is re-written as:

$$\ln[P(|k|)] = \ln[A] - 2z_t(k) \tag{3}$$

In equation 3 slope equals to $2z_t(k)$. If equation 2 is divided by 2, the linear estimation model can be obtained.

$$\ln\left[P(|k|)^{1/2}\right] = C - z_t(k) \tag{4}$$

where C is constant. The slope of equation 4 provides depth to the top of the magnetic layer ($z_t(k)$). Multiplying equation 1 by $e^{-|k|(z_0-z_0)}$ and dividing by 2 presents:

$$\ln\left[P(|k|)^{1/2}\right] = Ae^{-|k|z_0}\left(e^{-|k|(z_t-z_0)} - e^{-|k|(z_b-z_0)}\right) \tag{5}$$

where z_0 is depth to the centroid of the magnetic source and it is calculated as $(z_b-z_t)/2$. In order to compute z_b (CPD), z_0 must be calculated accurately and reliably. Replacing the exponential term in equation 5 by first terms of their Taylor series expansion produces approximated equation for z_0.

$$\ln\left[P(|k|)^{1/2}\right] \approx Ae^{-|k|z_0}(z_b - z_t) \tag{6}$$

($z_b - z_t$) is defined as the thickness of the magnetic crust [Buddington and Lindsley, 1964; Gasparini et al., 1979; Hunt et al., 1995; Nishitani and Kono, 1983; Salazar et al., 2017]. Substituting and rearranging thickness of the magnetic crust by z_0 yields:

$$\ln\left[\frac{P(|k|)^{1/2}}{|k|}\right] = \ln[D] - z_0|k| \tag{7}$$

In equation 7, D is constant and z_0 is computed from the slope for the low wavenumber components. Centroid depth of the magnetic layer is associated with the bottom of the magnetic layer [Okubo et al., 1985; Tanaka et al., 1999]:

$$z_b = 2z_0 - z_t \tag{8}$$

The magnetic anomaly map for CPD calculation is divided into 60 blocks with a size of 60 km×60 km. Each block is overlapped with an adjacent block by 50%. In other words, the distance of the centres of the two blocks to each other is 30 km. The centres of the blocks are shown with a black plus (Figure 2b). The power spectrum method of

Block No	blok center-X	blok center-Y	z_0	z_t	CPD (km)	Surface_heat Flow (mW/m²)		
						K = 2.5	K = 1.5	K = 1
b1	390790	3786850	10.37	1.8	18.94	76.6	45.9	30.6
b2	420790	3786850	11.19	2.48	19.9	72.9	43.7	29.1
b3	450790	3786850	9.04	1.8	16.28	89.1	53.4	35.6
b4	480790	3786850	13.26	1.73	24.79	58.5	35.1	23.4
b5	510790	3786850	8.95	1.51	16.39	88.5	53.1	35.4
b6	540790	3786850	13.36	2.18	24.54	59.1	35.5	23.6
b7	570790	3786850	14.39	1.86	26.92	53.9	32.3	21.5
b8	600790	3786850	13.92	2.02	25.82	56.2	33.7	22.5
b9	630790	3786850	9.06	2.13	15.99	90.7	54.4	36.3
b10	660790	3786850	13.26	1.69	24.83	58.4	35.0	23.4
b11	390790	3816850	11.11	1.98	20.24	71.6	43.0	28.7
b12	420790	3816850	7.73	1.72	13.74	105.5	63.3	42.2
b13	450790	3816850	7.73	1.54	13.92	104.2	62.5	41.7
b14	480790	3816850	10.97	1.7	20.24	71.6	43.0	28.7
b15	510790	3816850	10.77	1.9	19.64	73.8	44.3	29.5
b16	540790	3816850	15.33	2.48	28.18	51.5	30.9	20.6
b17	570790	3816850	12.43	2.02	22.84	63.5	38.1	25.4
b18	600790	3816850	8.74	1.98	15.5	93.5	56.1	37.4
b19	630790	3816850	12.62	1.8	23.44	61.9	37.1	24.7
b20	660790	3816850	13.62	1.88	25.36	57.2	34.3	22.9
b21	390790	3846850	14.58	3.36	25.8	56.2	33.7	22.5
b22	420790	3846850	13.97	3.16	24.78	58.5	35.1	23.4
b23	450790	3846850	8.49	1.7	15.28	94.9	56.9	38.0

Block No	blok center-X	blok center-Y	z_0	z_t	CPD (km)	Surface_heat Flow (mW/m²)		
						K = 2.5	K = 1.5	K = 1
b24	480790	3846850	11.51	1.91	21.11	68.7	41.2	27.5
b25	510790	3846850	10.89	1.92	19.86	73.0	43.8	29.2
b26	540790	3846850	11.36	2.41	20.31	71.4	42.8	28.6
b27	570790	3846850	10.37	1.88	18.86	76.9	46.1	30.8
b28	600790	3846850	8.2	1.92	14.48	100.1	60.1	40.1
b29	630790	3846850	10.54	2.29	18.79	77.2	46.3	30.9
b30	660790	3846850	12.98	2.4	23.56	61.5	36.9	24.6
b31	390790	3876850	15.58	2.89	28.27	51.3	30.8	20.5
b32	420790	3876850	9.94	2.22	17.66	82.1	49.3	32.8
b33	450790	3876850	7.46	1.65	13.27	109.3	65.6	43.7
b34	480790	3876850	10.13	1.57	18.69	77.6	46.5	31.0
b35	510790	3876850	8.75	2.04	15.46	93.8	56.3	37.5
b36	540790	3876850	9.02	1.72	16.32	88.8	53.3	35.5
b37	570790	3876850	7.77	1.65	13.89	104.4	62.6	41.8
b38	600790	3876850	8.7	2.02	15.38	94.3	56.6	37.7
b39	630790	3876850	11.1	2.63	19.57	74.1	44.5	29.6
b40	660790	3876850	9.42	1.94	16.9	85.8	51.5	34.3
b41	390790	3906850	12.52	2.11	22.93	63.2	37.9	25.3
b42	420790	3906850	9.17	1.96	16.38	88.5	53.1	35.4
b43	450790	3906850	9.37	1.91	16.83	86.2	51.7	34.5
b44	480790	3906850	8.02	2.22	13.82	104.9	63.0	42.0
b45	510790	3906850	9.28	2.06	16.5	87.9	52.7	35.2
b46	540790	3906850	9.76	2.13	17.39	83.4	50.0	33.4
b47	570790	3906850	10.52	1.77	19.27	75.2	45.1	30.1
b48	600790	3906850	9.3	1.76	16.84	86.1	51.7	34.4
b49	630790	3906850	12.43	1.74	23.12	62.7	37.6	25.1
b50	660790	3906850	10.17	1.77	18.57	78.1	46.8	31.2
b51	390790	3936850	8.84	1.69	15.99	90.7	54.4	36.3
b52	420790	3936850	9.94	1.76	18.12	80.0	48.0	32.0
b53	450790	3936850	9.36	1.86	16.86	86.0	51.6	34.4
b54	480790	3936850	8.13	1.81	14.45	100.3	60.2	40.1
b55	510790	3936850	8.98	1.78	16.18	89.6	53.8	35.8
b56	540790	3936850	7.14	1.88	12.4	116.9	70.2	46.8
b57	570790	3936850	8.78	1.82	15.74	92.1	55.3	36.8
b58	600790	3936850	11.67	1.7	21.64	67.0	40.2	26.8
b59	630790	3936850	13.92	2.11	25.73	56.4	33.8	22.5
b60	660790	3936850	14.04	2.21	25.87	56.0	33.6	22.4

Table 1. Curie Point Depths (CPD) and heat flow for the study area with block center coordinates and z_0, z_t, values.

Spector and Grant [1970] was applied to each block. Through the power spectra, z_t and z_0 were determined by the least-squares method. Calculated depths are given in Table 1. As an example, the power spectrum of the magnetic anomaly of block b16 is given in Figure 3. After the centre depth (z_0) of the deepest magnetic source is obtained, the upper boundary depth (z_t) of the magnetic source is estimated from the slope of the second-longest wavelength part of the spectrum. (Fig. 3a, 3b). Centre (z_0) and top (z_t) depths were computed as 15.33 km and 2.48 km for block b16. CPD was obtained as 28.18 km using Equation 8.

The calculation of heat flow and thermal gradient based on Fourier Law [1955] is given in equation 2. In this equation, it is assumed that the direction of the heat flow is vertical and the heat gradient dT/dZ is constant.

$$q = k\frac{dT}{dz},$$

(9)
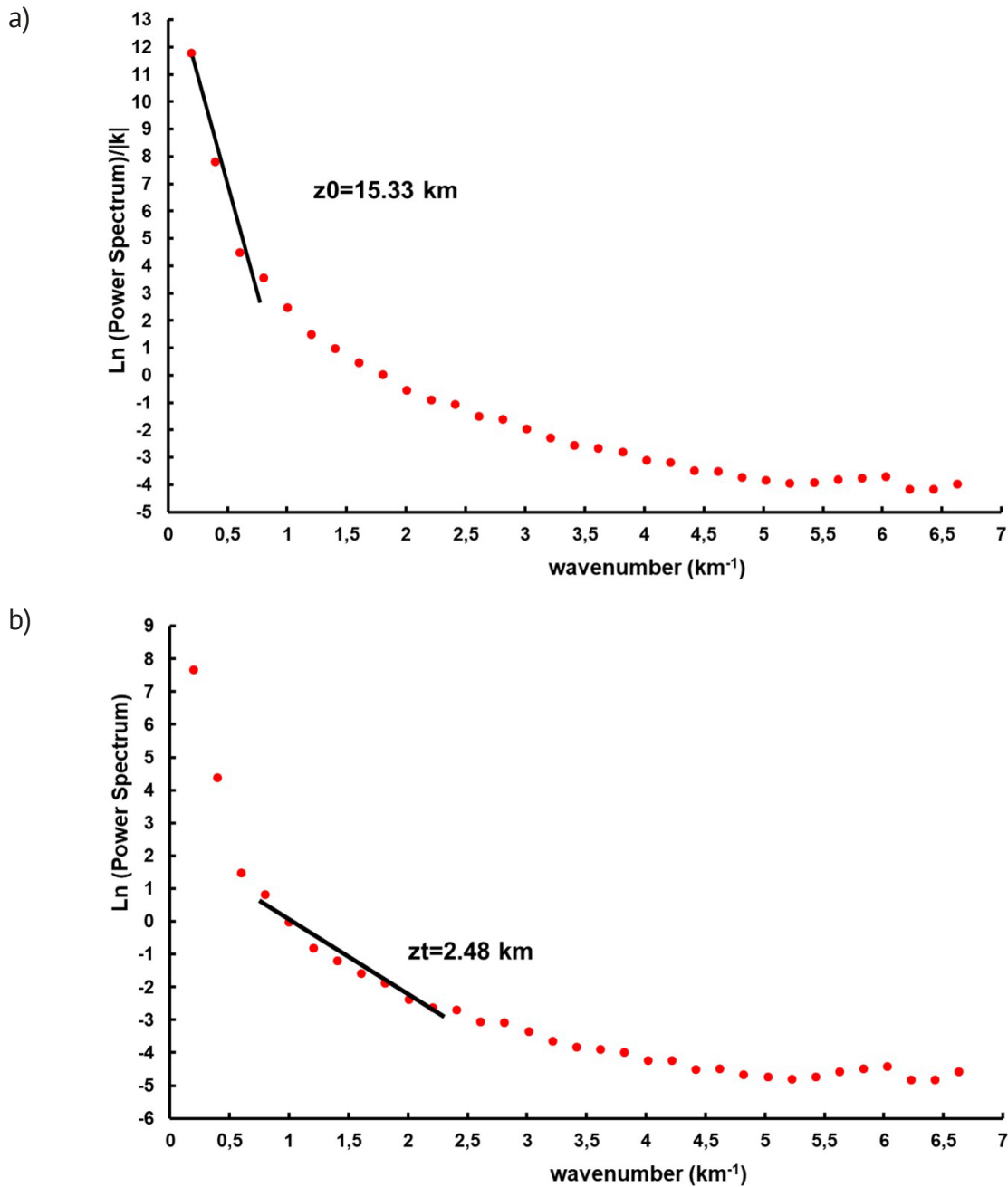
Figure 3. Examples of power spectrum of the block 16 for estimation of the CPD, a) the determining of the centroid depth, z_0 b) the determining of the top depth, z_t.

where q is heat flow, $\frac{dT}{dz}$ is thermal gradient, k is the coefficient of thermal conductivity. According to Tanaka et al. [1999], Curie temperature (θ) can be determined as (Eq 10):

$$\theta = \left[\frac{dT}{dz}\right] z_b, \tag{10}$$

where z_b is CPD. The heat flow values were obtained by combining Eqs. (9) and (10):

$$q = k\frac{\theta}{z_b}, \tag{11}$$

where q is heat flow, k is the coefficient of thermal conductivity, z_b is CPD. In heat flow calculation, it is assumed that thermal conductivity is 2.5 $Wm^{-1}K^{-1}$, Curie point temperature of 580 °C [Bektaş et al., 2007; Nwankwo et al. 2011; Pamuk 2019]. In addition, heat flow computation was made for K value 1 and 1.5 $Wm^{-1}K^{-1}$ in this study.

2.3.1 Wavenumber Ranges for the Estimated CPD

The computed z_b and z_t values should be validated by comparing theoretical approximation and linear estimation. Most of the authors ignore this comparison and select the wavenumber ranges manually. Núñez Demarco et al. [2021] evaluated 72 articles in terms of the wavenumber ranges. Núñez Demarco et al. [2021] suggested mathematical validity of computation can be tested by comparing the results of equations (2) and (3) for z_t and (5) and (6) for z_b. Comparison can be conducted by slope difference between linear estimation model and theoretical curve.

$$\Delta m = \left[\frac{t(k_{i+1}) - t(k_i)}{k_{i+1} - k_i} - \frac{l(k_{i+1}) - l(k_i)}{k_{i+1} - k_i}\right], \tag{12}$$

where Δm represents slope difference, $t(k)$ is the theoretical curve and $l(k)$ is the linear estimation. As Δm converges to 0, it is possible to say that the estimated z_0 and z_t are valid. In other words, the wavenumber ranges, where the difference between linear approximation and the theoretical curve is less than 5%, are valid for z_0 and z_t estimation. Broadly speaking, valid regions of z_t is larger than that of z_0. As the thickness of the magnetic layer (ΔZ) increases, valid regions tend to be wider for z_t and narrower for z_0. Moreover, if z_t is deeper for the constant ΔZ, the confidence region becomes broader.

2.4 Edge Detection in Magnetic Data

An attempt was made to determine the boundaries of the source causing the magnetic anomaly using Analytic Signal (AS), Total Horizontal Derivative (TDHR) and Tilt angle (TA) methods, which are the function of derivatives in the x, y or z directions of the potential field data. First, the approximate boundaries of the structures that cause the magnetic anomaly are determined by the Analytic Signal (AS) given in equation 13 [Nabighian, 1972; MacLeod et al., 1993; Bilim et al., 2017].

$$AS = \sqrt{\left(\frac{\partial M}{\partial x}\right)^2 + \left(\frac{\partial M}{\partial y}\right)^2 + \left(\frac{\partial M}{\partial z}\right)^2}, \tag{13}$$

where M is the magnitude of the magnetic anomaly and $\partial M/\partial x$ and $\partial M/\partial y$ are the horizontal derivatives, $\partial M/\partial z$ is the vertical derivative of the magnetic anomaly.

The second method used to determine the boundaries of geological structures is THDR developed by Cordell and Grauch [1985]. THDR can be determined using equation 14:

$$THDR = \sqrt{\left(\frac{\partial M}{\partial x}\right)^2 + \left(\frac{\partial M}{\partial y}\right)^2}, \tag{14}$$

The last method used for boundary analysis is the tilt angle developed by Miller and Singh [1994]. TA can be easily determined using equation 15.

$$TA = tan^{-1}\left(\frac{\frac{dM}{dz}}{THDR}\right), \tag{15}$$

where TA is tilt angle, $\partial M/\partial z$ is the vertical derivative of the magnetic anomaly, THDR is the total horizontal derivative. Tilt angle varies from –1.570 to 1.570 (–$\pi/2$ to +$\pi/2$). The TA values are negative outside the source while TA values are zero at the boundary location of the source in the vertical position.

2.5 Computation of Moho Depth

Airy-Heiskanen Isostasy theory is used for the estimation of Moho depth in the study area. Fundamentally, the theory assumes that topographic features are compensated by subsurface variations [Kirby, 2019]. According to Airy [1855] and Heiskanen [1931], crust-mantle boundary fluctuates regarding to significant undulations on the surface. It is worth noting that it is assumed that uniform densities are observed in both crust and mantle.

The compensation column can be described as the depth at which lithostatic pressures are uniform. The compensation depth is at the bottom of the lithospheric block, which is floating in the asthenosphere [Mukherjee, 2017]. For Airy-Heiskanen Isostasy theory, load lies directly under the topographic features and is not affected by neighbouring topographic loads [Liu et al., 2017]. Haxby and Turcotte [1978] suggested that the standard thickness of the crust with zero topographic elevation is usually taken as 30 km.

The equation of the Airy-Heiskanen Isostasy model is different for land and sea. For sea and land, the model can be described as:

$$t_{sea} = \frac{z_{bath}\,(\rho_{c-}\rho_w)}{(\rho_{M-}\rho_c)} + T, \tag{16}$$

$$t_{land} = \frac{z_{bath}\,\rho_c}{(\rho_{M-}\rho_c)} + T, \tag{17}$$

where t_{sea} and t_{land} are crust thickness for land and sea. Density in crust ρ_c, water (ρ_w) and Moho (ρ_M) are assumed as 2.67 g/cc, 1.03 g/cc and 3.30 g/cc respectively. T denotes compensation column from mean sea level and presumed as 30 km.

2.6 Cross-Correlation

Cross-correlation compares two series and provides the quantitative representation that indicates the degree of match [Bourke, 1996]. In this study, normalised 2D cross-correlation is preferred to compare Moho and Curie depths. Therefore, two gridded data are compared instead of series. Since the cross-correlation equation is normalised, the output will range from –1 to 1. The empirical description [Bourke, 1996] of cross-correlation for two gridded data ($x(i,j)$ and $y(i,j)$) is presented as:

$$r(i,j) = \frac{\sum_i \sum_j \left[\{x(i,j) - \overline{x(\iota,j)}\} \times \{y(i,j-d,u) - \overline{y(\iota,j)}\}\right]}{\sqrt{\sum_i \sum_j \{x(i,j) - \overline{x(\iota,j)}\}^2} \times \sqrt{\sum_i \sum_j \{y(i,j) - \overline{y(\iota,j)}\}^2}}, \tag{18}$$

where $\overline{x(\iota,j)}$ and $\overline{y(\iota,j)}$ are mean values of two gridded datasets, d and u are lags. If the output of the normalised cross-correlation is 1 or –1, it is likely to say that the two datasets are positively or negatively correlated. Nevertheless, 0 or approximately 0 cross-correlation value represents uncorrelated datasets.

3. Results

RTP magnetic anomaly map of the study area was investigated. The RTP anomalies are centred over magnetic sources which provide a more interpretable map in terms of causative bodies. RTP only take the phase of the magnetic field into account instead of the amplitude of the field. RTP has required for edge detection and depth estimation methods except for analytic signal and local wavenumber [Fairhead et al., 2011].

It was observed that magnetic values ranged from –202 to 413 nT. The lowest magnetic values (negative anomalies) were observed in the east of the Polis and Paphos regions, and the highest magnetic values were obtained in the west and east of the Rizokarpaso region in the east of Nicosia and Kyrenia. Values in the west of the Rizokarpaso (Dipkarpaz) region range from 140 to 400 nT (Figure 2b). It is possible to say that lower magnetic values in the RTP map may correspond to the thinner magnetic crust where lower CPD or high heat flow are values observed. However, this assumption is not valid in all areas since the primary factor that effect the strength field is magnetic mineral content in the subsurface.

The distribution of other CPD values obtained for Cyprus Island and its surroundings is given in Table 1 and Figure 4. CPD values range from 12.4 km to 28.18 km for the study area. Maximum CPD values were obtained at
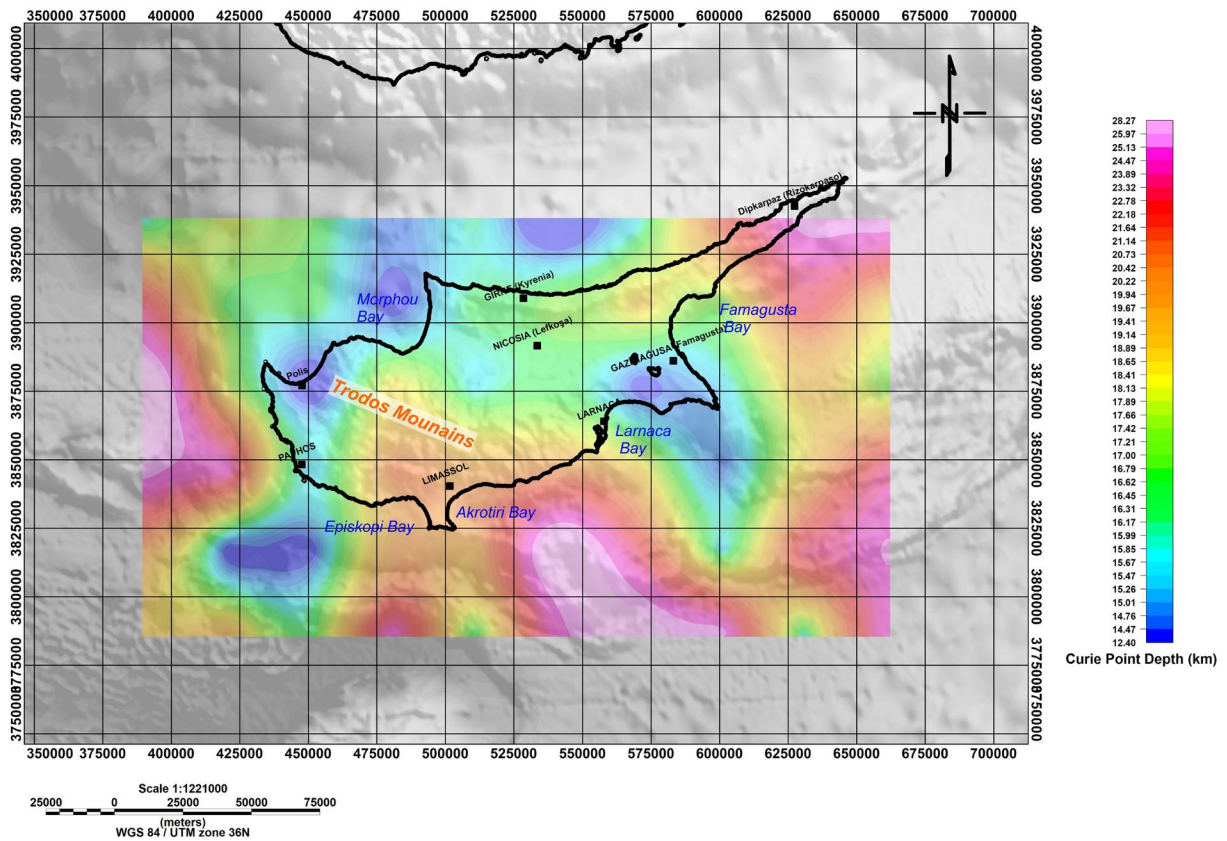

Figure 4. Curie Point Depth (CPD) map of Cyprus Island.

the southeast of Akrotiri Bay, west of the study area, around Rizokarpaso (Dipkarpaz). CPD values in these areas are deeper than 25 km. The shallowest CPD values were obtained around Polis, Morphou Bay, in the area between Larnaca and Famagusta and north of Kyrenia. CPD values in these areas are shallower than 15 km. CPD values range from 18 to 20 km in Limassol, and range from 15 to 18 km in Nicosia (Lefkoşa) and south of it, around Kyrenia, and west of Famagusta (Figure 4).

Heat Flow values were calculated based on CPD values, and these calculated values were given in Figure 5 and Table 1. Heat flow values (for K = 2.5 Wm^{-1}K^{-1}) were calculated between 51.3 and 116.0 mW/m^2 for the study area (Figure 5). Minimum heat flow values were obtained to the west of the study area, southeast of Akrotiri Bay, around Rizokarpaso (Dipkarpaz), and southeast of the study area. Heat flow values are less than 65 mW/m^2 in these areas. The highest heat flow values were obtained around Polis, Morphou Bay, in the area between Larnaca and Famagusta and north of Kyrenia. Heat flow values are more than 100 mW/m^2 in these areas. Moreover, Heat flow values range from 65 to 75 mW/m^2 around Limassol, and range from 85 to 95 mW/m^2 in Nicosia and south of it, around Kyrenia, west of Famagusta (Figure 5).
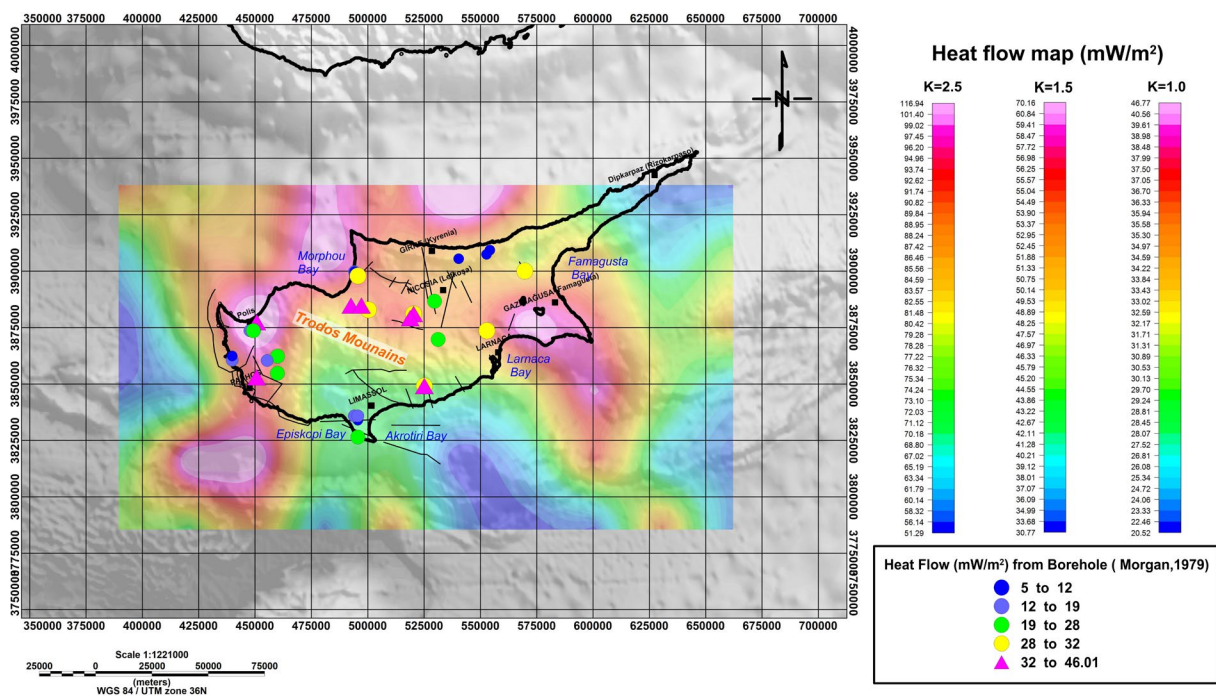

Figure 5. Heat-flow map of Cyprus Island for thermal conductivity 2.5 Wm^{-1}K^{-1}; 1.5 Wm^{-1}K^{-1} and 1 Wm^{-1}K^{-1} [with heat flow values from boreholes, Morgan, 1979].

In this study, AS, THDR and TA methods were used to detect the boundaries (geological contacts, faults, etc.) of the structures that cause magnetic anomalies in and around the study area. Maximum and minimum values of AS and THDR ranges from 0.0002 to 0.0537 and 0 to 0.0394 respectively. The AS and THDR maps present higher values in the NW part of the study area while lower values are observed in the SE part. TA values vary between +1.57 rad (90°) and –1.57 rad (–90°). The higher TA values are noted in the NW, NE and S part of the study area whilst SE and E parts have lower TA values.

4. Discussion and Conclusion

In this study, CPD and heat flow were obtained for Cyprus Island by spectral analysis of EMAG2 magnetic data. In addition, the boundaries of geological structures, which play an important role in interpreting potential field data, are defined by different edge detection techniques. First, reduction to the pole was applied to the magnetic

data, and then generated magnetic anomaly map was divided into 60 parts for CPD calculation. CPD and heat flow values were calculated for each block and mapped. CPD values ranged from 12.4 km to 28.18 km, and heat flow values were calculated between 20 and 50 mW/m² for K = 1. Low CPD values and high heat flow values can potentially be associated with geothermal fields. Therefore, areas with high heat flow and low CPD value may be recommended for further geothermal research. Structure boundaries obtained by boundary analysis methods (AS, THDR, TA) are generally compatible with each other.

The estimated CPD values are justified by comparing theoretical and linear approximation models for different magnetic thicknesses. The confidence region corresponds to areas where slope difference $< 5\%$. The range of the estimated z_t is from 1.51 km to 3.36 km. Furthermore, the average thickness of the magnetic layer is 25 km. Since the minimum z_t for the constant ΔZ corresponds to the narrowest confidence region, 1.51 km is chosen to test the validity of the estimations (Figure 6). For $z_t = 1.51$ km and $\Delta Z = 25$ km, the valid region covers $\text{k} > 0.72$ km^{-1} is valid for z_t estimation whereas confidence region for z_0 is $\text{k} < 0.71$ km^{-1}. During the estimation process wavenumber range for z_t is from 0.79 km^{-1} to 2.50 km^{-1} while the same range for z_0 is between 0.13 km^{-1} and 0.69 km^{-1}. It is possible to say that z_t and z_0 values are computed within the mathematically appropriate region.
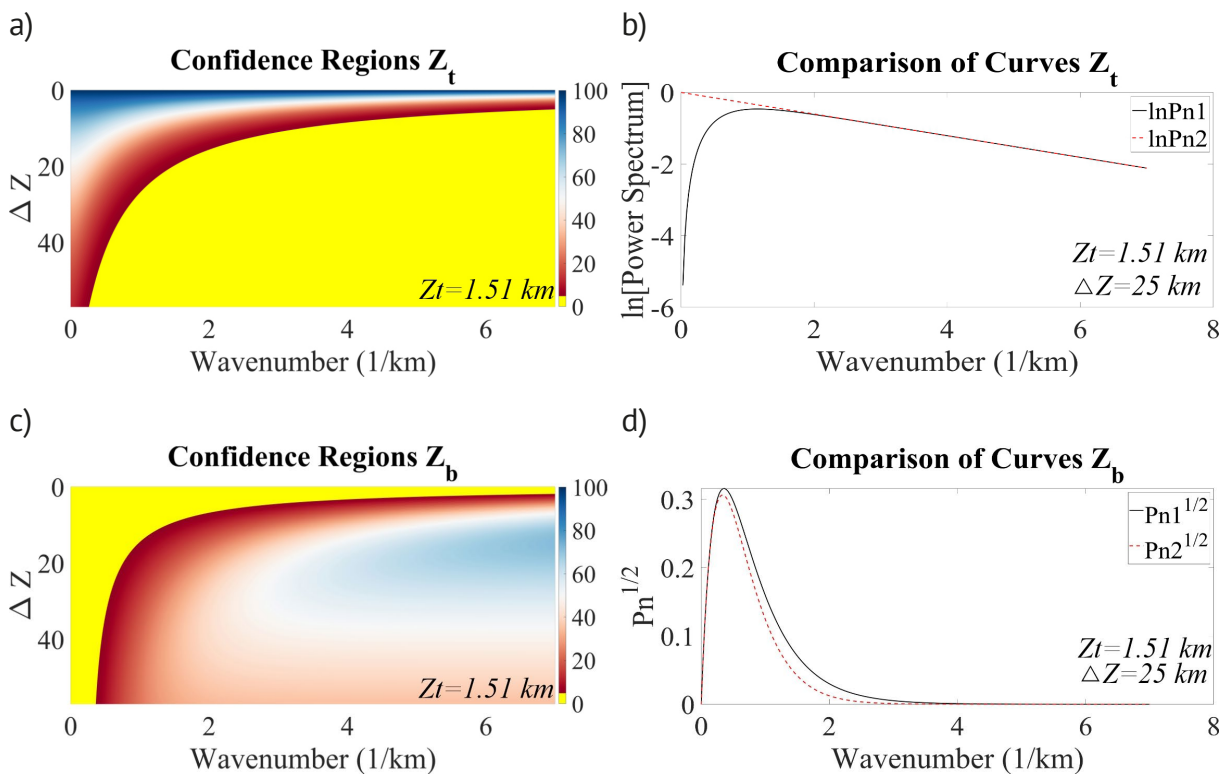

Figure 6. Comparison of theoretical curve and linear approximation: a) Slope difference (%) map for z_t estimation, b) Correlation between theoretical and linear approximation model for z_t computation, c) Slope difference (%) map for z_0 estimation, d) Correlation between theoretical and linear approximation model for z_0 computation.

Losif Stylianou et al. [2017] focused on a methodology to measure and analyze the thermal properties of lithology in their study. They obtained thermal conductivity between 0.5 and 1.5 Wm^{-1}K^{-1} for Nicosia (Lefkoşa). Florides et al. [2014] presented information about the density, thermal conductivity, specific heat, and thermal diffusivity of various lithologies in Cyprus Island. They calculated thermal conductivity at different values for different samples. They noted that the specific weight of the rocks is the cause of this. For example, they measured 0.50 Wm^{-1}K^{-1} for Nicosia marl, and 2.29 Wm^{-1}K^{-1} for Serpentinite, and 0.82 Wm^{-1}K^{-1} for Upper pillow Lava. In another study, Florides et al. [2010] calculated thermal conductivity values as follows; 1.42 to 1.97 Wm^{-1}K^{-1}, for Lakatamia 1.68 Wm^{-1}K^{-1}, Agia Napa 1.58 Wm^{-1}K^{-1}, Meneou 1.4 to 1.72 Wm^{-1}K^{-1}, and Prodromi 1.87 Wm^{-1}K^{-1}. Losif Stylianou et al. [2016] presented a thermal conductivity map for Cyprus Island in the studies they conducted

in 2016. In their study, estimated thermal conductivity values range from 0.6 to 4.5 $Wm^{-1}K^{-1}$. In his study, Morgan [1979] reported that thermal conductivity is lower than 2 $Wm^{-1}K^{-1}$ in general terms for Cyprus. Since the K value is very variable for Cyprus, the heat flow calculation was calculated for the cases where the thermal conductivity is 2.5, 1.5 and 1 $Wm^{-1}K^{-1}$ and shown in Figure 5. Morgan [1979] also performed heat flow calculations for Cyprus with the help of 33 boreholes. These heat flow calculations were also given in Figure 5 and compared with the heat flow values calculated in this study. Morgan [1979] observed the best fit value as K = 1 $Wm^{-1}K^{-1}$ amongst the heat flow values he calculated and the heat flow values obtained in this study.

For K = 1, the heat flow values ranged from 20 to 50 mW/m^2 in this study, and the heat flow values ranged from 5 to 46 mW/m^2 in Morgan's study [1979]. Morgan [1979] calculated between 28-32 mW/m^2 in Larnaca, and it was 35 mW/m^2 in this study. The heat flow values measured in the wells between Polis and Paphos were between 5 and 46 mW/m^2, and the heat flow in this region ranges from 35-40 mW/m^2 in this study. The heat flow was between 28-46 mW/m^2 in the well measurements in the old study at the northeast of the Troodos mountains, and in this study, the heat flow in this area was about 35 mW/m^2. Heat flow measurements in wells at the southwest of Limassol were between 5 and 28 mW/m^2, and in this study, these values in the same area are around 25 mW/m^2. It can be said that the results of this study are consistent with older [Morgan, 1979] well studies in general terms for these areas mentioned. The heat flow was between 5-12 mW/m^2 in the wells at the east of Kyrenia, and The heat flow in this area was obtained as 30 mW/m^2 in this study. The results are incompatible with older studies for this region (Figure 5). In addition, Kalogirou [2014] prepared a heat flow map for Cyprus Island using artificial neural networks in their study. In this study, the map they created was consistent with areas with high heat flow (Polis and its surroundings, Morphou Bay and its surroundings, Paphas and its surroundings).
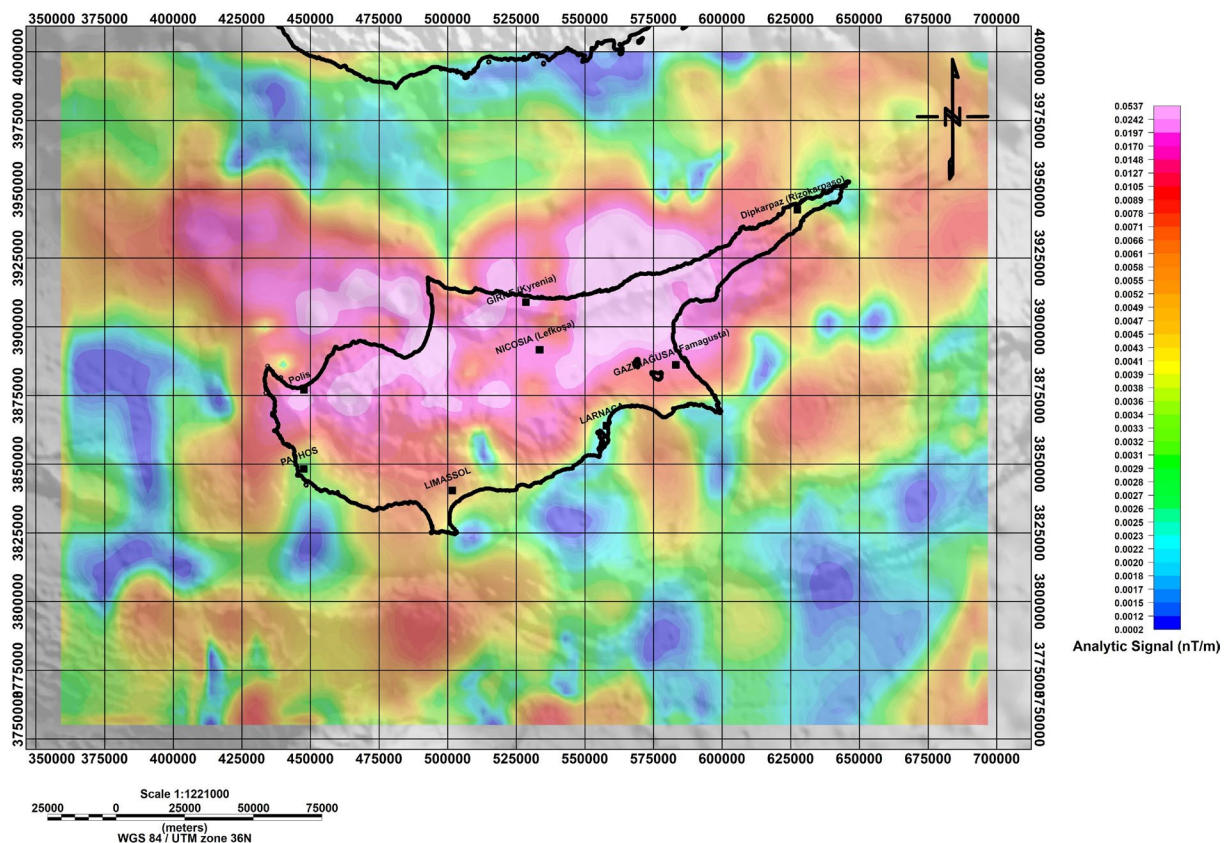

Figure 7. Analytic signal (AS) map of the magnetic anomaly of Cyprus Island.

In the AS map, maximum amplitudes were obtained at the west of Nicosia (Lefkoşa) and Kyrenia, and north of Famagusta (Figure 6). Regarding to the AS map, the structures that cause magnetic anomaly generally draw an arc between Rizokarpaso, Kyrenia, and Morphou Bay (Figure 7). THDR map was examined, and it showed similar results

to the AS map. In the west and east of Nicosia and Kyrenia, and north of Famagusta, the direction of the structure causing the magnetic anomaly was determined as N-S (Figure 8). As known in the TA distribution, zero contours are directly related to the structure boundary. The boundaries of the structure that caused magnetic anomaly were obtained as N-S, such as THDR in the west of Nicosia and Kyrenia, and north of Famagusta. The N-S structures was indicated by dashed circles. The structure that causes the anomaly in this area extends to the land boundary in the area between Larnaca and Famagusta. The structure boundaries were obtained by different orientations around the Troodos Mountains. The structure boundaries that start at the Episkoi and Akrotiti bays and extend to the southeast of the study area are NW-SE directional. In the NE of the study area, the structures are generally NE-SW directional (Figure 9).
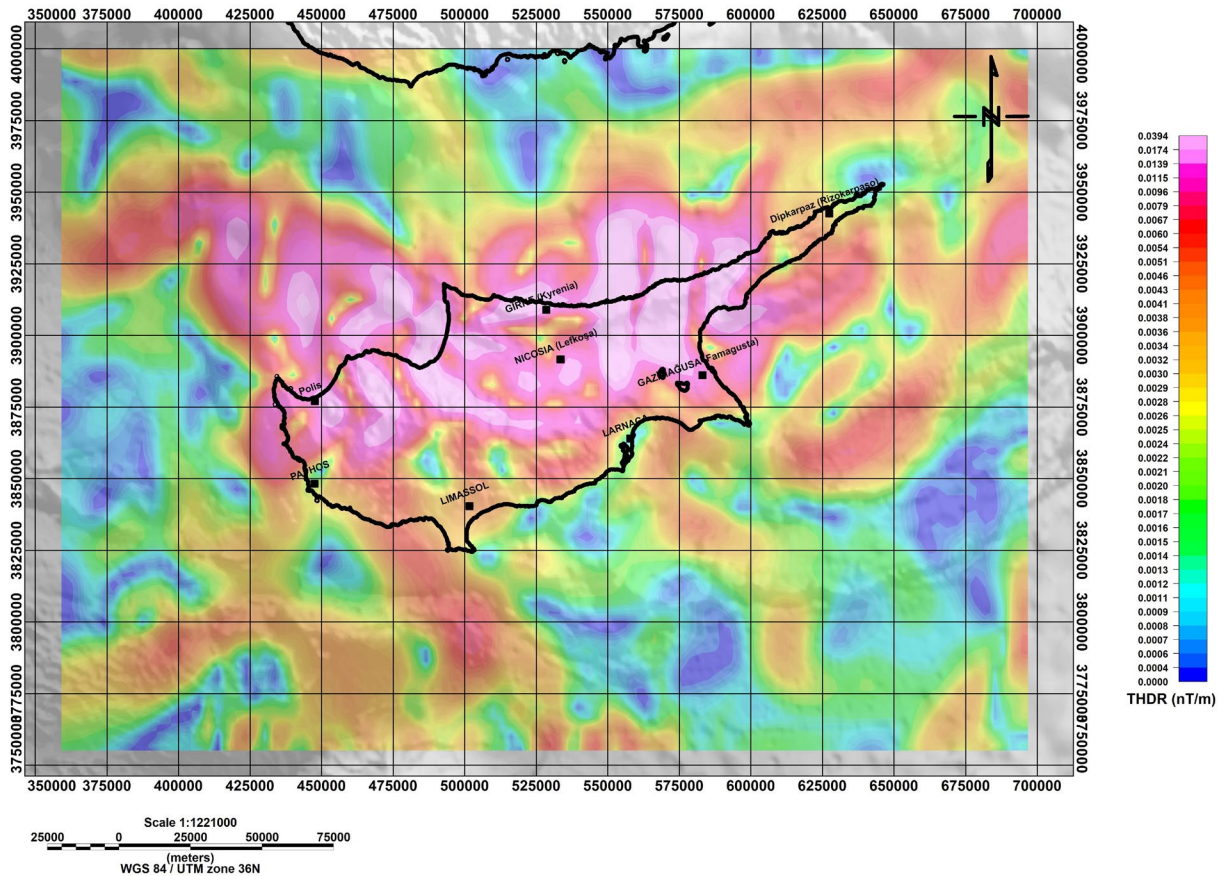

Figure 8. THDR (total horizontal derivative) map of the magnetic anomaly of Cyprus Island.

Moho depth and CPD are two physical situations that reflect temperature and discontinuity layer. However, both physical situations are indicating a boundary. CPD demonstrates the boundary between magnetic and nonmagnetic crust whereas Moho depth illustrates crust-mantle boundary. Moho depth can be considered as a boundary at which compositional change occurs. In some cases, especially in stable tectonic zones, magnetic rocks are substituted by non-magnetic rocks at these transition zones [Ravat et al., 2007]. As a result of this, the difference between Moho and Curie depths becomes close to 0 [Idárraga-García and Vargas, 2008; Özsöz, 2021]. Karabulut et al. [2019] was computed crustal thickness from receiver function analysis. According to their estimations, the crustal thickness in Cyprus Island is between 20 and 30 km. Furthermore, thicker crust is observed in the northern part of Cyprus Island which is compatible with Moho depth estimation results in this study.

Calculated Moho depth through the Airy-Heiskanen theory is compared to Curie depth to enhance interpretation of the tectonic activity. In order to analyse the tectonic regime of the area, correlation and difference between Moho and Curie depths are used. Additionally, cross-correlation of Moho and Curie is computed to evaluate the areas where Moho and Curie depths match remarkably. It is probable to say that if Moho and Curie considerably match,
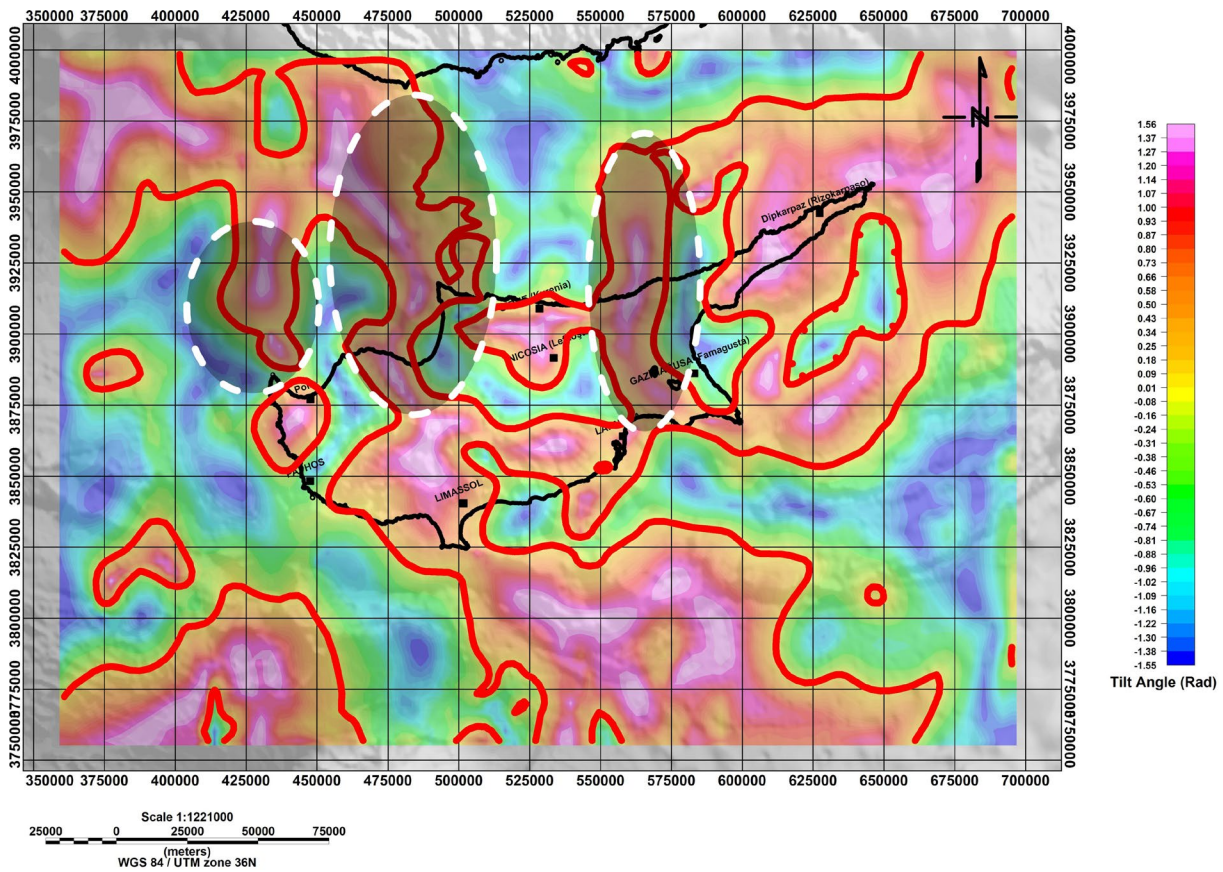
Figure 9. TA (Tilt Angle) map of the magnetic anomaly of Cyprus Island (red line shows 0 contour in TA map).

the region might be interpreted as a passive crust. On the other hand, the mismatch or notable difference between Moho and Curie is likely to indicate an active tectonic regime. Illustration of Curie depth, Moho depth, Moho-Curie and cross-correlation of Curie and Moho depths are given in Figure 10.

There are two reasons for obtaining shallower Moho depth than CPD. The first reason is the Moho-Curie difference is higher than 0 unless upper mantle magnetic phases are observed [Haggerty, 1978; Roberts, 2006; Ferré et al., 2013]. In that case, it is possible to say that the temperature of the magnetised mantle is lower than Curie temperature [Guimarães et al., 2014]. The second reason is that Curie depth estimation using spectral analysis is a fairly subjective process. Additionally, the Moho depth calculation approach includes assumptions that affect the result significantly. Hence, the unrealistic negative values may appear in the Moho-Curie difference due to subjectivity and the presumptions.

As it can be seen from Figure 10, Moho depth values are remarkably high (around 35-38 km) in Troodos Mountains due to the isostatic compensation theory. Curie depth values are relatively deeper (28-30 km) in the S-SE part of the study area. Regarding to cross-correlation results, a higher correlation coefficient (0.60-0.75) in the southern part of Cyprus Island is observed. Moho-Curie difference produced approximately 0 contours in the southern part of the study area. It is possible to say that the tectonically passive regime becomes dominant towards the southern part of the study area due to high cross-correlation values and low difference in that region.

It is crucial to note that earthquakes are generally occurring in the brittle part of the crust. Therefore, it is fair to say that both rigidity of the crust and Curie depth are dependent on temperature in the subsurface. Consequently, including the focal depth and distribution of the seismic activity would enhance the interpretation stage. Regarding the quantitative analysis of the earthquakes, mean focal depth and magnitude are 25.86 ± 16.06 km and 3.42 ± 0.64 respectively.

The earthquake distribution map and Moho-Curie should be associated since 0 contours of Moho-Curie represent passive tectonic activity. Spatial distribution of earthquake data indicates that the majority of tectonic activity occurs in the south-western part of Cyprus Island where the Moho-Curie difference is approximately 10 km. Few earthquakes are noted in the southern and the western part of the study area where Moho-Curie is around 0.
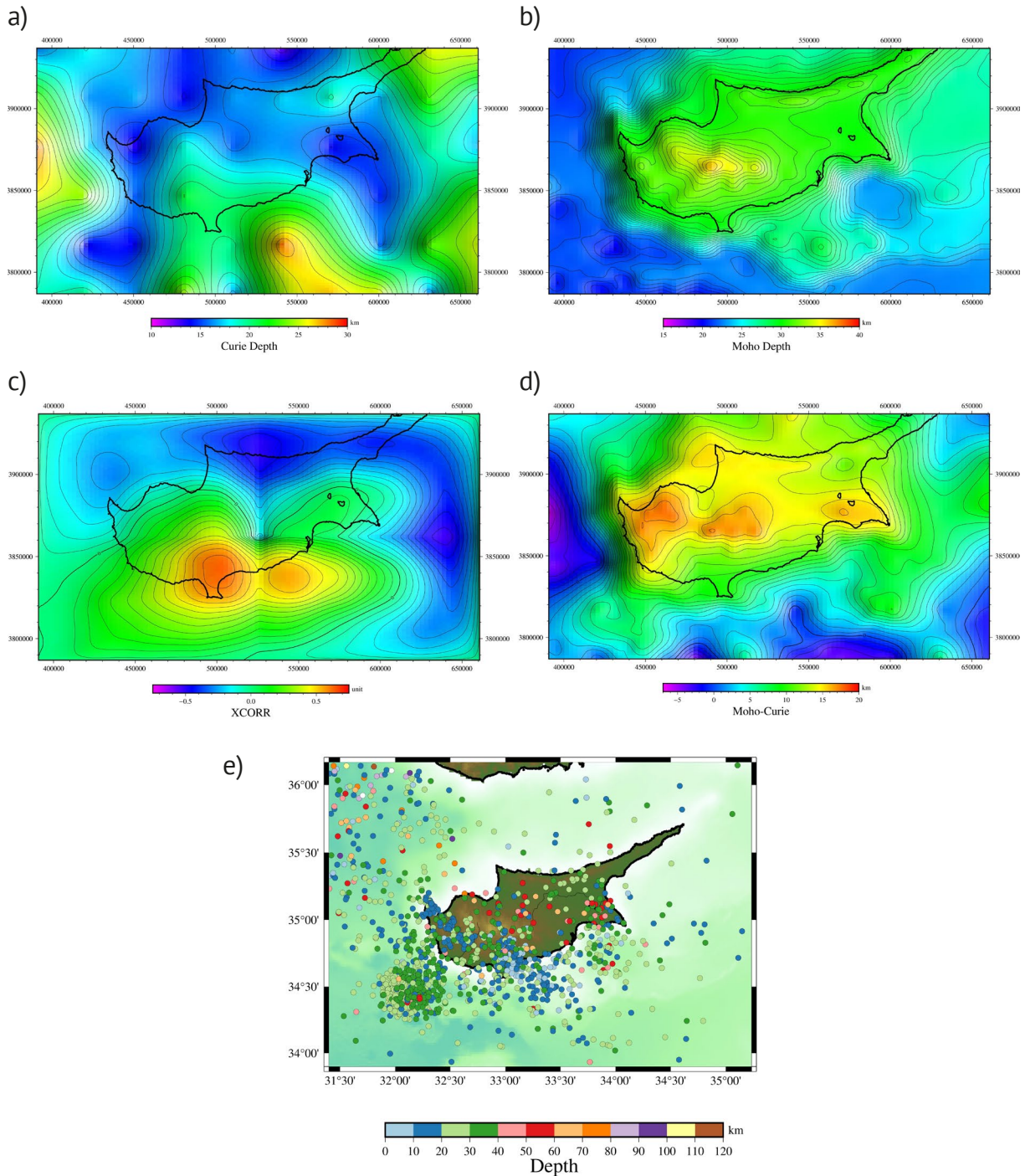
Figure 10. Interpretation of tectonic activity in the study area: a) Curie depth map, b) Moho depth map, c) cross-correlation between Moho and Curie depth maps, d) Map that obtained by subtracting Curie depth values from Moho depth values, e) Earthquake (M > 2.5) distribution map.

Conversely, if Moho-Curie is relatively high with respect to the surrounding region such as the south-western part of Cyprus Island, an abundant number of earthquakes are observed. The deeper earthquake activity (> 30 km) dominantly occurred in the southwestern part of the study area where Curie and Moho depths are relatively shallow. Moreover, this area corresponds to the convergent plate boundary in which deep tectonic activity tends to occur.

This work presents a tectonic interpretation of Cyprus Island by CPD estimation, edge detection methods, Moho-Curie comparison and spatial earthquake distribution. The findings of the study shed light on stable-unstable crustal structure and orientation of the magnetic sources in the study area. The AS, THDR and TA results showed that N-S oriented structure is observed in the west and east of Kyrenia (Girne) and Nicosia (Lefkoşa). However,

17

the orientation of the magnetic anomaly is not identical around the Troodos Mountains for these edge detection methods. Combined analysis of Moho and Curie depths showed that stable crustal characteristics are observed in the southern part of the study area. There is a large number of earthquakes are noted in the south-western part of the study area where the Moho-Curie difference relatively high.

References

Airy, G.B. (1855). III. On the computation of the effect of the attraction of mountain-masses, as disturbing the apparent astronomical latitude of stations in geodetic surveys, Philosophical Trans. Royal Soc. Lon., 145, 101-104.

Arnaiz-Rodríguez, M.S., N. Orihuela (2013). Curie point depth in Venezuela and the Eastern Caribbean, Tectonophysics, 590, 38-51.

Asim, K. M., S. S. Moustafa, I.A. Niaz, E.A. Elawadi, T. Iqbal, F. Martinez-Alvarez (2020). Seismicity analysis and machine learning models for short-term low magnitude seismic activity predictions in Cyprus, Soil Dyn. Earthq. Engin., 130, 105932.

Bektaş, Ö., D. Ravat, A. Büyüksaraç, F. Bilim, A. Ateş (2007). Regional geothermal characterisation of East Anatolia from aeromagnetic, heat flow and gravity dataì, Pure Appl. Geophys., 164, 5, 975-998.

Bilim, F., S. Kosaroglu, A. Aydemir, A. Buyuksarac (2017). Thermal investigation in the Cappadocia region, Central Anatolia-Turkey, analyzing curie point depth, geothermal gradient, and heat-flow maps from the aeromagnetic data, Pure Appl. Geophys. 174, 12, 4445-4458.

Bhattacharyya, B.K. and L.K. Leu (1975). Spectral analysis of gravity and magnetic anomalies due to two-dimensional structures, Geophysics, 40, 6, 993-1013.

Blakely, R.J. (1995). Potential theory in gravity and magnetic applications, Cambridge University Press.

Blome, C.D. and W.P. Irwin (1985). Equivalent radiolarian ages from ophiolitic terranes of Cyprus and Oman, Geology, 13, 401-404.

Bourke, P., (1996). Cross correlation, autocorrelation, 2d pattern identification. Research Gate, 2019.

Buddington, A.F. and D.H. Lindsley (1964). Iron-titanium oxide minerals and synthetic equivalents, J. Petrol., 5, 2, 310-357.

Cagnan, Z. and G.B. Tanircan (2010). Seismic hazard assessment for Cyprus, J. Seismol., 14, 2, 225-246.

Chukwu, C.G., E.E. Udensi, E.M. Abraham, A.C. Ekwe, A.O. Selemo (2018). Geothermal energy potential from analysis of aeromagnetic data of part of the Niger-delta basin, southern Nigeria, Energy, 143, 846-853.

Connard, G., R. Couch and M. Gemperle (1983). Analysis of aeromagnetic measurements from the Cascade Range in central Oregon, Geophysics, 48, 3, 259-401.

Cordell, L. and V.J.S. Grauch (1985). Mapping basement magnetization zones from aeromagnetic data in the San Juan Basin, New Mexico, In The utility of regional gravity and magnetic anomaly maps, 181-197, Society of Exploration Geophysicists (SEG).

Elmas, A. (2018). Determination of Structural Discontinuities in Cyprus Island by Using EGM08 Gravity Data, J. Geol. Engin., 42, 1, 17-32 (in turkish).

Ergün, M., S. Okay, C. Sari and E.Z. Oral (2003). April. Gravity and magnetic anomalies of the Cyprus arc and tectonic implications, In EGS-AGU-EUG Joint Assembly, 1663.

Fairhead, J.D., A. Salem, L. Cascone, M. Hammill, S. Masterton and E. Samson (2011). New developments of the magnetic tilt-depth method to improve structural mapping of sedimentary basins, Geophys. Prosp., 59, Advances in Electromagnetic, Gravity and Magnetic Methods for Exploration, 1072-1086.

Ferré, E.C., S.A. Friedman, F. Martín-Hernández, J.M. Feinberg, J.A. Conder, and D.A. Ionov (2013). The magnetism of mantle xenoliths and potential implications for sub-Moho magnetic sources, Geophys. Res. Lett., 40, 1, 105-110.

Florides, G. A., I. Iosif-Stylianou, Z. Zomeni, E. Tsiolakis, P. Pouloupatis, S. A. Kalogirou, V. Messarites, Z. Zomeni, E. Tsiolakis, P.D. Pouloupatis, E. Theofanous (2014). Thermal properties of the ground in Cyprus and their correlations and effect on the efficiency of ground heat exchangers, Int. J. Environ., Ecol., Geol. Marine Engin., 8, 2, 112-116.

Florides, G.A., P. Pouloupatis, S.A. Kalogirou, V. Messaritis, I. Panayides, Z. Zomeni, G. Partasides, A. Lizides E. Eleni Sophocleous, K. Koutsoumpas (2010). Temperature profiles and thermal properties of the ground in Cyprus, for use in the design of ground heat exchangers, In Euro Sun 2010.

Fourier, J. (1955). Analytical Theory of Heat, Dover Publications, New York.

Gasparini, P., M.S.M. Mantovani, G. Corrado and A. Rapolla (1979). Depth of Curie temperature in continental shields: a compositional boundary?. Nature, 278, 5707, 845-846.

Guimarães, S.N.P., D. Ravat and V.M. Hamza (2014). Combined use of the centroid and matched filtering spectral magnetic methods in determining thermomagnetic characteristics of the crust in the structural provinces of Central Brazil, Tectonophysics, 624, 87-99.

Haggerty S.E. (1978). Mineralogical constraints on Curie isotherms in deep crustal magnetic anomalies, Geophys. Res. Lett., 5, 105e108, https://doi.org/ 10.1029/GL005i002p00105.

Hakyemez, H.Y. (2014). Main geological characterıstıcs of Northern Cyprus, TAPG Bulletin, 26, 2, 7-46, (in turkish).

Heiskanen, W. (1931). Isostatic tables for the reduction of gravimetric observations calculated on the basis of Airy's hypothesis, Bulletin Géodésique, 30, 1, 110-153.

Harrison, R. W., W. L. Newell, H. Batıhanlı, I. Panayides, J. P. McGeehin, S. A. Mahan, A. Ozhur E. Tsiolaki, M. Necdet (2004). Tectonic framework and Late Cenozoic tectonic history of the northern part of Cyprus: implications for earthquake hazards and regional tectonics, J. Asian Earth Sci., 23, 2, 191-210.

Haxby, W.F. and D.L. Turcotte (1978). On isostatic geoid anomalies, J. Geophys. Res.: Solid Earth, 83, B11, 5473-5478.

Hunt, C.P., B.M. Moskowitz and S.K. Banerjee (1995). Magnetic properties of rocks and minerals. Rock physics and phase relations: A handbook of physical constants, 3, 189-204.

Idárraga-García, J. and C.A. Vargas (2018). Depth to the bottom of magnetic layer in South America and its relationship to Curie isotherm, Moho depth and seismicity behavior, Geod. Geodyn., 9, 1, 93-107.

Kalogirou, S. A., P. Christodoulides, G. A. Florides, P. Pouloupatis, I. Iosif-Stylianou (2014). Using Artificial Neural Networks for the construction of contour maps of thermal conductivity, Adv. Neural Net., Fuzzy Sys. Artificial Intel., 95-99, ISBN: 978-960-474-379-7

Karabulut, H., A. Paul, A.D. Özbakır, T. Ergün, and S. Şentürk (2019). A new crustal model of the Anatolia-Aegean domain: evidence for the dominant role of isostasy in the support of the Anatolian plateau, Geophys. J. Int., 218, 1, 57-73.

Kempler, D. and Z. Ben-Avraham (1987). The tectonic evolution of the Cyprean Arc, Ann. Tecton., 1, 58-71.

Kinnaird, T.C. (2008). Tectonic and sedimentary response to oblique and incipient continental collision the easternmost Mediterranean (Cyprus), unpublished Phd thesis, University of Edinburgh.

Kirby, J.F. (2019). On the pitfalls of Airy isostasy and the isostatic gravity anomaly in general, Geophys. J. Int., 216, 1, 103-122.

Kumar, S., S.K. Pal, A. Guha, S.D. Sahoo, A. Mukherjee (2020). New insights on Kimberlite emplacement around the Bundelkhand Craton using integrated satellite-based remote sensing, gravity and magnetic data, Geocarto Int., 1-23.

Li, C.F., J. Wang (2016). Variations in Moho and Curie depths and heat flow in Eastern and Southeastern Asia, Marine Geophys. Res., 37, 1, 1-20.

Li, C.F., Y. Lu, J. Wang (2017). A global reference model of Curie-point depths based on EMAG2, Scientific Rep. 7, 1, 1-9.

Liu, B., Y. Zhou, and G. Yang (2017). Characteristics of isostatic gravity anomaly in Sichuan-Yunnan region, China, Geod. Geodyn., 8, 4, 238-245.

MacLeod, I.N., K. Jones and T.F. Dai (1993). 3-D analytic signal in the interpretation of total magnetic field data at low magnetic latitudes, Explor. Geophys., 24, 679-688.

Makris, J., Z.B. Abraham, A. Behle, A. Ginzburg, P. Giese, L. Steinmetz, R.B. Whitmarsh and S. Eleftheriou (1983). Seismic refraction profiles between Cyprus and Israel and their interpretation, Geophys. J. Int., 75, 3, 575-591.

Maus, S., F. Yin, H. Lühr, C. Manoj, M. Rother, J. Rauberg, I. Michaelis, C. Stolle, and R.D. Müller (2008). Resolution of direction of oceanic magnetic lineations by the sixth-generation lithospheric magnetic field model from CHAMP satellite magnetic measurements, Geochem., Geophys., Geosys, 9, 7, https://doi.org/10.1029/2008GC001949.

Maus, S., U. Barckhausen, H. Berkenbosch, N. Bournas, J. Brozena, V. Childers, F. Dostaler, J.D. Fairhead, C. Finn, R.R.B von Frese, C. Gaina, S. Golynsky, R. Kucks, H. Lühr, P. Milligan, S. Mogren, R.D. Muller, O. Olesen, M. Pilkington, R. Saltus, B. Schreckenberger, E. Thebault and F.C. Tontini (2009). EMAG2: A 2-arc min resolution Earth Magnetic Anomaly Grid compiled from satellite, airborne, and marine magnetic measurements. Geochemistry, Geophysics, Geosystems 10, 8, https://doi.org/10.1029/2009GC002471

McPhee, P.J. and D.J. van Hinsbergen (2019). Tectonic reconstruction of Cyprus reveals Late Miocene continental collision of Africa and Anatolia, Gondwana Res., 68, 158-173.

Miller, H.G. and V. Singh (1994). Potential field tilt - a new concept for location of potential field sources., J. Appl. Geophys., 32, 213-217.

Mohammed, A., T. Adewumi, S. A. Kazeem, R. Abdulwaheed, A.A. Adetona, A. Usman (2019). Assessment of geothermal potentials in some parts of upper Benue Trough northeast Nigeria using aeromagnetic data, J. Geosci., Engin., Env., Technol., 4, 1, 7-15.

Montadert, L., S. Nicolaides, H.P. Semb, O. Lie (2014). Petroleum Systems Offshore Cyprus, in Petroleum systems of the Tethyan region, edited by L. Marlow, C. Kendall and L. Yose, AAPG memoir 106, 301-334.

Morgan, P. (1979). Cyprus heat flow with comments on the thermal regime of the eastern Mediterranean. In Terrestrial heat flow in Europe (Springer, Berlin, Heidelberg, 144-151.

Mukasa, S.B., J.N. Ludden (1987). Uranium-lead isotopic ages of plagiogranites from the Troodos ophiolite, Cyprus, and their tectonic significance, Geology, 15, 9, 825-828.

Mukherjee, S. (2017). Airy's isostatic model: a proposal for a realistic case, Arabian J. Geosci., 10, 12, 1-7.

Nabighian, M.N. (1972). The analytic signal of two-dimensional magnetic bodies with polygonal cross-section: its properties and use for automated anomaly interpretation, Geophysics, 37, 507-517.

Nagata, T. (1961). Rock magnetism, Maruzen, Tokyo. Nnange, J. Mining, Poudjom Djomani 350.

Nishitani, T. and M. Kono (1983). Curie temperature and lattice constant of oxidized titanomagnetite, Geophys. J.Int., 74, 2, 585-600.

Njeudjang, K., J. D. Kana, A. Tom, J.M.A. Essi, N. Djongyang, R. Tchinda (2020). Curie point depth and heat flow deduced from spectral analysis of magnetic data over Adamawa volcanic region (Northern Cameroon): geothermal implications, SN Appl. Sci., 2, 8, 1-16.

Núñez Demarco, P., C. Prezzi, and L. Sánchez Bettucci (2021). Review of Curie point depth determination through different spectral methods applied to magnetic data, Geophys. J. Int., 224, 1, 17-39.

Nwankwo, L. I., P.I. Olasehinde and C.O. Akoshile (2011). Heat flow anomalies from the spectral analysis of airborne magnetic data of Nupe Basin, Nigeria, Asian J. Earth Sci., 4, 1, 20-28.

Okubo, Y., R.J. Graf, R.O. Hansen, K. Ogawa, H. Tsu (1985). Curie-point depths of the Island of Kyushu and surrounding areas, Japan, Geophysics, 50, 481-494.

Özer, Ç., S. Öztürk, E. Pamuk (2022). Tectonic and structural characteristics of Erzurum and its surroundings (Eastern Turkey): a detailed comparison between different geophysical parameters. Turkish J. Earth Sci., 31, 85-108.

Özsöz, İ. (2021). Combined qualitative and quantitative regional interpretation of the thermal results of magnetic data in the Eastern Mediterranean Region, Turkish J. Earth Sci., 30, 5, 665-680.

Pamuk, E. (2019). Investigating edge detection, Curie point depth, and heat flow using EMAG2 magnetic and EGM08 gravity data in the northern part of Eastern Anatolia, Turkey, Turkish J. Earth Sci., 28, 6, 805-821.

Ravat, D., A. Pignatelli, I. Nicolosi and M. Chiappini (2007). A study of spectral methods of estimating the depth to the bottom of magnetic sources from near-surface magnetic anomaly data, Geophys. J. Int., 169, 2, 421-434.

Roberts, A.P. (2006). High-resolution magnetic analysis of sediment cores: strengths, limitations and strategies for maximizing the value of long-core magnetic data, Phys. Earth Planet. Int., 156, 3-4, 162-178.

Robertson, A.H. (1998). Mesozoic-Tertiary tectonic evolution of the easternmost Mediterranean area: integration of marine and land evidence, In Proceedings of the Ocean Drilling Program, Scientific Results, 160, 54.

Ross, H.E., R.J. Blakely and M.D. Zoback (2006). Testing the use of aeromagnetic data for the determination of Curie depth in California, Geophysics, 71, 5, L51-L59.

Salazar, J.M., C.A. Vargas and H. Leon (2017). Curie point depth in the SW Caribbean using the radially averaged spectra of magnetic anomalies, Tectonophysics, 694, 400-413.

Spector, A. and F.S. Grant (1970). Statistical models for interpreting aeromagnetic data, Geophysics, 35, 2, 293-302.

Staudigel, H., K.M. Gillis, R. Duncan (1986). K/Ar and Rb/Sr ages of celadonites from the Troodos ophiolite, Cyprus, Geology 14, 72-75.

Stylianou, I.I., G. Florides, S. Tassou, E. Tsiolakis, P. Christodoulides (2017). Methodology for estimating the ground heat absorption rate of Ground Heat Exchangers. Energy 127, 258-270.

Stylianou, I.I., S. Tassou, P. Christodoulides, I. Panayides, G. Florides (2016). Measurement and analysis of thermal properties of rocks for the compilation of geothermal maps of Cyprus, Renew. Ener. 88, 418-429.

Swarbrick, R.E., A.H.F. Robertson (1980). Revised stratigraphy of the Mesozoic rocks of southern Cyprus, Geol. Mag., 117, 06, 547, https://doi.org/10.1017/S0016756800028892.

Symeou, V. (2018). Transition from compression to strike-slip tectonic styles along the northern margin of the Levant Basin Doctoral dissertation, Sorbonne université.

Tanaka, A., Y. Okubo, O. Matsubayashi (1999). Curie point depth based on spectrum analysis of the magnetic anomaly data in East and Southeast Asia, Tectonophysics, 306, 3-4, 461-470.

Treitel, S., W.G. Clement, and R.K. Kaul (1971). The spectral determination of depths to buried magnetic basement rocks, Geophys. J. Int., 24, 4, 415-428.

Ulutaş, E. (2020). The May 11 Paphos, Cyprus, earthquake: implications for stress regime and tsunami modelling for the Eastern Mediterranean shorelines, Arabian J. Geosci., 13, 18, 1-13.

USGS (2021). Earthquake Catalogue [online]. Website https://earthquake.usgs.gov/earthquakes/search/ [accessed 25 August 2021].

Xu, Y., T. Hao, H. Zeyen, F. Nan (2017). Curie point depths in North China Craton based on spectral analysis of magnetic anomalies, Pure Appl. Geophys., 174, 1, 339-347.

Zissimos, A.M., I.C. Christoforou, D.R. Cohen, S.D. Mooney, N.F. Rutherford (2019). Spatial distribution and controls on organic and inorganic carbon in the soils of Cyprus, J. Geochem. Expl., 196, 95-104.

*CORRESPONDING AUTHOR: Eren PAMUK,

Department of Geophysical Research, General Directorate of the Mineral Research & Exploration of Turkey, 06800, Ankara, Turkey,

e-mail: eren.pamuk@mta.gov.tr